**ORIGINAL PAPER**

# First-principles investigations on the formation of H₂O defects in lizardite with influence on the elastic property

Shichuan Sun[1,2] · Yu He[1,3]

HPSTAR
866-2019

## Abstract

Dehydration of hydrous minerals is the key for understanding the partial melting and earthquakes taking place at subduction zones. It has been reported that a large amount of H₂O defects (HD) can be formed during the dehydration process. However, the HD effects on the properties of hydrous minerals have never been considered previously. In this work, density functional theory (DFT) calculations were carried out to study the formation enthalpies of HD in lizardite. The calculated formation enthalpies of lizardite with 0.8125 wt% HD are below 0.5 eV at pressures from 0 to 7 GPa, which are low enough for the formation of HD, especially at high temperature. The presence of HD exerts significant influence on the elastic property of lizardite, resulting in lower seismic velocities and obviously higher seismic velocity anisotropy. We also calculated the migration barrier energy of $H^+$, $Mg^{2+}$, and $Si^{4+}$ in lizardite. $H^+$ migration barrier energy is 1.16 eV (vertical with ⟨001⟩ direction) and 3.40 eV (along ⟨001⟩ direction) at the pressure of 3 GPa, while Mg and Si present much higher values of more than 5 and 9 eV, respectively. Further simulations of first-principles molecular dynamics (FPMD) on lizardite with and without HD indicate that the crystal structure of HD-bearing lizardite is thermodynamically stable, and proton conduction is not obvious in lizardite and HD-bearing lizardite at temperatures below 900 K and pressures below 2 GPa.

**Keywords** Lizardite · H₂O defects · Elastic property · Seismic anomalies

## Introduction

Serpentine is the main hydrous mineral stored in forearc mantle and subduction zones, and is associated with subducting slab dehydration, the water cycle, partial melting, and deep and intermediate earthquakes, and is crucial for understanding electrical and seismic anomalies in Earth's interior (Reynard 2013; Hyndman and Peacock 2003). Serpentine is well classified into three main species, i.e., lizardite, having a flat layer

✉ Yu He
  heyu@mail.gyig.ac.cn

1  Key Laboratory of High-Temperature and High-Pressure Study of the Earth's Interior, Institute of Geochemistry, Chinese Academy of Sciences, Guiyang 550081, Guizhou, China

2  University of Chinese Academy of Sciences, Beijing 100049, China

3  Center for High Pressure Science and Technology Advanced Research, Shanghai 201203, China

structure; antigorite, having a corrugated layer structure; and chrysotile, having a cylindrical layer structure (Whittaker and Zussman 1956). The stability of lizardite was once the subject of heated debate among petrologists (Evans 1977; Frost 1975; Dungan 1979; Caruso and Chernosky 1979). However, it has been consistently concluded that lizardite forms as low-grade metamorphic serpentine in low-temperature, slow-diffusion environments, while antigorite is the predominant species of serpentine in high-temperature, high-pressure (Padrón-Navarta et al. 2010), and high-grade metamorphic rock terranes (Auzende et al. 2006). Antigorite can be stable in the field up to temperatures of 600 °C, while lizardite and chrysotile may form in relative low-temperature regions mostly below 20 km depth (Reynard et al. 2011). Although the stable regions of lizardite are poorly constrained, the large quantities and extensive distributions make it a significant serpentine phase (Caruso and Chernosky 1979). The phase transition and dehydration mechanisms of serpentine are well studied (Evans 2004; Schwartz et al. 2013; Auzende et al. 2015), which suggests the similar conclusion.

Previous studies of the electrical conductivity of lizardite suggested that lizardite is an insulator below 300 °C

and before dehydration (Zhu et al. 2001). Its high electrical conductivity at higher temperatures is attributed to fluid flow generated by dehydration (Reynard et al. 2011; Zhu et al. 2001), and conduction of lizardite is attributed to proton conduction (Guo et al. 2011).

Evidence of the dehydroxylation reaction of brucite has been reported in early experimental investigations (Freund and Sperling 1976; El-Salaam et al. 1979). McKelvy et al. (2001) reported direct observations of a stable lamellar mineral with HD-bearing structure and presented evidence for partial dehydration of lamellar-structured minerals arising from the dehydroxylation reaction. HD may occur in hydrous minerals having similar structures as brucite. Among hydrous minerals, lizardite is a potential candidate mineral to contain partial dehydration and form HD-bearing structures, because it possesses a similar flat lamellar structure to brucite, with 1:1 alternating oxide and hydroxide layers. The dehydroxylation mechanism in lizardite has been investigated and analyzed in multiple experiments (Brindley and Zussman 1957; Dlugogorski and Balucan 2014; Seipold and Schilling 2003), providing direct evidence of partial dehydration and HD formation in lizardite. Thermal dehydroxylation of lizardite was also investigated by simulation of X-ray diffraction patterns (McKelvy et al. 2006), which are consistent with previous experiments.

There has been minimal attention given to the effects of HD on the properties of hydrous minerals under conditions of high pressures and temperatures (*P–T*). Here, we performed first-principles calculations to investigate lizardite and the effects of HD on ionic transport properties, electric conductivity, and seismic velocities of lizardite under conditions of high *P–T* (0–7 GPa and 0–900 K).

## Method

### Equation of state and HD formation enthalpies

To obtain the equation of state, we employed density functional theory (Kohn and Sham 1965), and all computational jobs were performed within Vienna ab initio simulation package (VASP) (Kresse and Furthmüller 1996). In this study, we performed DFT calculations with generalized gradient approximation (GGA) (PBE: Perdew and Zunger 1981), which presents better accuracy than local density approximation (LDA) in calculating energetic and elastic properties of hydrous minerals (Mookherjee and Mainprice 2014; Mookherjee and Tsuchiya 2015; Tsuchiya and Tsuchiya 2009a, b; Tsuchiya et al. 2002, 2005). We set seven groups of calculations corresponding to different HD rates, respectively, and unit cell of lizardite. Lizardite, $(Mg_3Si_2O_5(OH)_4)$, with different HD rates of 4.33, 3.25, 2.17, 1.625, and 0.8125 wt% were generated by two HD defects in a $3 \times 1 \times 1$ supercell and one HD defect in a $2 \times 1 \times 1$, $3 \times 1 \times 1$, $2 \times 2 \times 1$ and $2 \times 2 \times 2$ supercell, respectively. The space group of HD-bearing lizardite changed from P31 m into triclinic. Detailed formation mechanism of HD is exhibited in Fig. 1.

As shown in Fig. 1a, 0.8125 wt% lizardite and HD structure kept stable in the calculations. The coordination number of Mg around the HD changed from 6 to 5 (Fig. 1b). The energy cut-off was tested and a common $E_{CUT}$ of 520 eV was established. The H (1 $s^1$), O ($2s^22p^4$), Mg (3 $s^2$), and Si ($3s^23p^23d^0$) orbits were treated as valence states. The k-point meshes of lizardite were sampled on a $5 \times 5 \times 4$ gamma point grid, while HD-bearing lizardite with different HD rates of 4.33, 3.25, 2.17, 1.625, and 0.8125 wt% were sampled on a $2 \times 5 \times 4$, $2 \times 4 \times 3$, $2 \times 5 \times 4$, $2 \times 2 \times 3$ and $2 \times 2 \times 2$ gamma point grid, respectively. We first fully relaxed the structure with PBE pseudopotential at zero pressure, using a conjugate gradient minimization until all the forces acting on ions were less than 0.01 eV/Å per atom, and then, we calculated the *E–V* relationship by setting a series of constant volumes during structure relaxing.

Each group was tested within 7 GPa, considering of the stable depth for store and dehydration. The final results of *E–V* data were fitted to a third-order Birch–Murnaghan equation of state (EOS):



**Fig. 1** Formation mechanism of $H_2O$ defects in lizardite. **a**, **b** Snapshot of 0.8125 wt% HD-bearing lizardite of (100) and (001) direction. Red, Pink, red, golden, and blue spheres represent H, O, Mg, and Si atoms, respectively
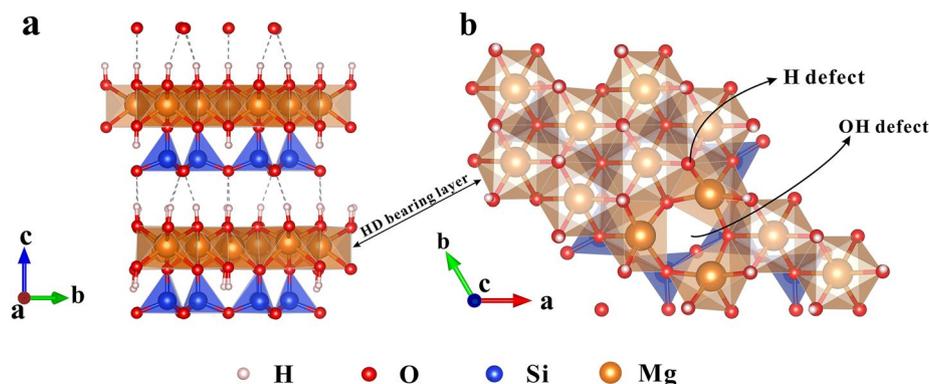
$$E(V) = E_0 + \frac{9V_0 B_0}{16} \left\{ \left[ \left( \frac{V_0}{V} \right)^{\frac{2}{3}} - 1 \right]^3 B_0' \right.$$

$$\left. + \left[ \left( \frac{V_0}{V} \right)^{\frac{2}{3}} - 1 \right]^2 \left[ 6 - 4 \left( \frac{V_0}{V} \right)^{\frac{2}{3}} \right] \right\}. \tag{1}$$

The $P$–$V$ relation is derived from the equation expressed below:

$$P(V) = \frac{3B_0}{2} \left[ \left( \frac{V_0}{V} \right)^{\frac{7}{3}} - \left( \frac{V_0}{V} \right)^{\frac{5}{3}} \right]$$

$$\times \left\{ 1 + \frac{3}{4} (B_0' - 4) \left[ \left( \frac{V_0}{V} \right)^{\frac{2}{3}} - 1 \right] \right\}. \tag{2}$$

The method of investigating phase transition and reaction mechanism via relative enthalpy has already been well tested in hydrous phase (Tsuchiya 2013b).

## High $P$–$T$ stability and ionic transport property

First-Principles Molecular Dynamics (FPMD) was used to investigate the stability of HD-bearing lizardite under high $P$–$T$ and HD effects on proton conduction. A $2 \times 2 \times 2$ supercell containing 144 atoms was used for FPMD simulations. A cut-off energy of 400 eV was employed in this work, while the Brillouin zone sampling was performed at $\Gamma$ point. The equilibration step was first conducted in the canonical ensemble (NVT) employing a Nosé thermostat. For each temperature (500–900 K), molecular dynamics simulations were performed with 13,000 steps (13 ps) and the pressure normally distributed as a function of steps. We obtained the balanced pressure by averaging the pressure of 1.5–13 ps. The time-average mean-square displacements (MSD) (Mo et al. 2012) were derived from the equation below:

$$\langle [\vec{r}(t)] \rangle = \frac{1}{N} \sum_{i=1}^{N} \left\langle [\vec{r}_i(t - t_0) - \vec{r}_i(t_0)]^2 \right\rangle. \tag{3}$$

The $\vec{r}_i(t)$ denotes the displacement of the $i$th H or O or Mg or Si ion at time $t$, and $N$ is the total number of ions in the system.

The proton migration energy was calculated by climbing image-nudged elastic band (CINEB) method (Henkelman et al. 2000). A $2 \times 2 \times 2$ supercell containing 144 atoms was set for simulation. We adopted $\Gamma$ point for k-point sampling,

considering of the computational cost and by convergence check of denser case (He et al. 2016).

## Elasticity and seismic velocity

The elastic constant matrix $C_{ij}$ was calculated using the finite strain method (Karki et al. 1997, 2001). The crystal structure of mineral showed better fit with Hook's Law within 1% strain rate, which provides us a good approach to accurately obtain the elastic constants of crystal. The elastic properties of crystal are expressed as the relationship between stress and strain:

$$\sigma_{ij} = C_{ijkl} \varepsilon_{kl}, \tag{4}$$

where $\sigma_{ij}$ refers to stress tensor, $\varepsilon_{kl}$ refers to strain tensor, and $C_{ijkl}$ represents fourth order elastic modulus. Considering of the symmetry of $C_{ijkl}$, the equation is simplified as below:

$$\sigma_i = C_{ij} \varepsilon_j. \tag{5}$$

The equation could be expanded as follows:

$$\begin{pmatrix} \sigma 1 \\ \sigma 2 \\ \sigma 3 \\ \sigma 4 \\ \sigma 5 \\ \sigma 6 \end{pmatrix} = \begin{pmatrix} C11 & C12 & C13 & C14 & C15 & C16 \\ & C22 & C23 & C24 & C25 & C26 \\ & & C33 & C34 & C35 & C36 \\ & & & C44 & C45 & C46 \\ & & & & C55 & C56 \\ & & & & & C66 \end{pmatrix} \cdot \begin{pmatrix} \varepsilon 1 \\ \varepsilon 2 \\ \varepsilon 3 \\ \varepsilon 4 \\ \varepsilon 5 \\ \varepsilon 6 \end{pmatrix}. \tag{6}$$

For strain in different directions, each could be expressed in the form of Hooke's Law:

$$\Delta \sigma = k \cdot \Delta \varepsilon, \tag{7}$$

where k represents elastic coefficient. In each direction, strains were set, respectively, for $\varepsilon$ in $\pm 0.01, \pm 0.005, 0$, five group of strains were added by:

$$a' = a(I + \varepsilon), \tag{8}$$

where $\underline{a}$ represents third-order cell parameter matrix, and $\underline{\varepsilon}$ represents added strain $\Delta \varepsilon$, and $\underline{I}$ represents third-order identity matrix. The final results of strain–stress data were fitted to Eq. (7) employing central difference method. For each optimizing result, correlation coefficient $\gamma$ were controlled larger than 90% to get the exact elastic constants. Exceptionally, in the special orientation of $C_{ij}$ (table S1), $\gamma$ turns out within 90%, this was possibly attributed to the relative weak elasticity and correspond to a narrower range of elastic deformation. In this case, we diminished the strain range and optimize the elastic constant with $\varepsilon$ in $\pm 0.005$ to obtain high accuracy and reasonable results. To fully understood seismic properties of lizardite, we calculated the $V_P$, $V_S$ and $V_\emptyset$ using the Voigt–Ruess–Hill scheme (Voigt 1928; Reuss 1929; Hill 1952), which was defined as:

$$B = \frac{B_V + B_R}{2} \quad G = \frac{G_V + G_R}{2} \tag{9}$$

$$V_P = \sqrt{\frac{B + \frac{4G}{3}}{\rho}} \quad V_S = \sqrt{\frac{G}{\rho}} \quad V_\emptyset = \sqrt{\frac{B}{\rho}}, \tag{10}$$

where $B_V$ and $G_V$ denotes bulk modulus and shear modulus of Voigt model (Voigt 1928). $B_R$ and $G_R$ denote bulk modulus and shear modulus of Ruess model (Reuss 1929). $B$ denotes bulk modulus, $G$ is shear modulus, and $V_\emptyset$ denotes bulk sound velocity. To calculate the seismic anisotropy, we also need the velocities in different directions which can be obtained by solving the Christoffel equation (e.g., Anderson 1989; Karki et al. 1997):

$$\left| C_{ijkl} n_j n_l - \rho V^2 \delta_{ik} \right| = 0. \tag{11}$$

In high-symmetry directions, when polarization directions are parallel or vertical with the propagation directions of velocities, the modes are called pure longitudinal or transverse, respectively. In general directions, the velocities are divided into one quasi-longitudinal $V_P$(closet to propagation directions) and two spitting shear wave velocities, vertical with $V_P$, $V_{S1}$ (fast) and $V_{S2}$(slow). The seismic anisotropy of P-wave and S-wave are defined as:

$$AV_P = \frac{\left( V_P^{MAX} - V_P^{MIN} \right) \times 200}{\left( V_P^{MAX} + V_P^{MIN} \right)}. \tag{12}$$

In the formula, $V_P^{MAX}$ and $V_P^{MIN}$ are the maximum and minimum velocities of P-wave. Similarly, the anisotropy of S-wave is defined as:

$$AV_{S1} = \frac{\left( V_{S1}^{MAX} - V_{S1}^{MIN} \right) \times 200}{\left( V_{S1}^{MAX} + V_{S1}^{MIN} \right)} \tag{13}$$

$$AV_{S2} = \frac{\left( V_{S2}^{MAX} - V_{S2}^{MIN} \right) \times 200}{\left( V_{S2}^{MAX} + V_{S2}^{MIN} \right)}, \tag{14}$$

where $V_{S1}^{MAX}$ and $V_{S1}^{MAX}$ are the maximum and minimum velocities of $S_1$-wave(fast), while $V_{S2}^{MAX}$. and $V_{S2}^{MAX}$ are the maximum and minimum velocities of $S_2$-wave(slow).

In our FPMD calculations, the structure of lizardite and 0.8125 wt% HD-bearing lizardite kept hydrostatic at high $P$–$T$ condition of the temperature at 500, 700, and 900 K and the pressure around 1 GPa–2 GPa.

## Results and discussion

### Equation of state and HD formation enthalpies

We fitted the third-order Birch–Murnaghan equation of state (EOS) of lizardite with parameters $V_0 = 185.6$ Å$^3$, $B_0 = 42.20$ GPa, and $B_0' = 14.47$ GPa, values that are in close agreement

**Table 1** EOS results, calculated $V_0$, $E_0$, $B_0$, and $B_0'$ were listed in the table, and previous works were also listed for comparing

| HD rate (wt%) | $V$ (Å$^3$) | $B_0$ (GPa) | $B_0'$ | |
|---|---|---|---|---|
| This study (GGA) | | | | |
| – | 184.9 | 59.97 | 4 (fixed) | < 7 GPa, 0 K (this study) |
| – | 184.83 | 62.64 | 2.77 (fixed) | < 7 GPa, 0 K (this study) |
| – | 185.6 | 42.20 | 14.47 | < 7 GPa, 0 K (this study) |
| 4.33 | 188.36 | 22.07 | 20.60 | < 7 GPa, 0 K (this study) |
| 3.25 | 188.09 | 26.17 | 19.50 | < 7 GPa, 0 K (this study) |
| 2.17 | 186.56 | 33.77 | 14.59 | < 7 GPa, 0 K (this study) |
| 1.625 | 186.51 | 34.06 | 16.33 | < 7 GPa, 0 K (this study) |
| 0.8125 | 186.05 | 36.00 | 18.44 | < 7 GPa, 0 K (this study) |
| – | 186.34 | 41.36 | 12.38 | DFT. GGA, 0 K (< 7 GPa)[a] |
| – | 180.93 | 68.9 | 4 (fixed) | Exp. Synchrotron X-ray diffraction at 300 K[b] |
| – | 180.92 | 71.0 | 3.2 | Exp. Synchrotron X-ray diffraction at 300 K[b] |
| – | 182.3 | 76.4 | 2.39 | Calc. GGA, 0 K[c] |
| – | 184.06 | 63.5 | 2.77 | Shock wave[d] |
| – | 178.40 | 57.0 | – | SCXRD[e] |

[a]Theoretical data at 0 K, < 7 GPa, and taken from Mainak Mookherjee et al. (2009)

[b]Experiment data performed by Hilairet et al. (2006)

[c]Theoretical calculation, at 0 K, Tsuchiya et al. (2013a)

[d]Experiment of shock wave method, Tyburczy et al. (1991)

[e]SCXRD experiment data provided by Mellini and Zanazzi (1989)

with those values calculated by Mookherjee and Stixrude (2009) and Tsuchiya (2013a). The fitted parameters of $B_0 = 62.64$ GPa and $V_0 = 184.83$ Å$^3$ are almost the same as the shock wave experiment results when $B_0'$ is fixed to 2.77 (Tyburczy et al. 1991). The derived results are also consistence with the SCXRD data (Mellini and Zanazzi 1989) and experiment of synchrotron X-ray diffraction (Hilairet et al. 2006). The parameters of EOS for lizardite with different HD concentrations are calculated and shown in Table 1. The bulk modulus $B_0$ dramatically declines with the increasing concentrations of HD in lizardite.

The derived $P$–$V$ relations are presented in Fig. 2a. The calculated $P$–$V$ relation of lizardite in this study shows good consistence with the calculation results (GGA) of Mookherjee and Stixrude (2009) and the situ compression experimental data provided by Hilairet et al. (2006). HD-bearing lizardite shows steeper slope as the concentration of HD increasing, which are related to the decreasing bulk modulus $B_0$. To further understand energy changes in the process of defect generation, we calculated the total enthalpies before and after the generation of defects at a temperature of 0 K. The enthalpies of lizardite and HD-bearing lizardite were obtained from the $H$–$V$ relationships, which were derived from $E$–$V$ relationships. Then, we compared the total enthalpies of the products and the reactants to determine the activation enthalpy of the dehydroxylation reaction, as shown in Eq. (15). The enthalpies of $H_2O$(VIII) were obtained under the same conditions and all the enthalpies of lizardite in different HD

concentrations were normalized to unit cell for analyzing. The relative enthalpies were derived from the equation below:

$$H_{form} = H_{HD} + H_{H_2O} - H_{Liz}. \tag{15}$$

As shown in Fig. 2b, the HD formation enthalpies increase steadily as the pressure increasing. For HD concentration of 0.8125 wt%, the average formation enthalpy of HD is below 0.5 eV, which is low enough for HD formation in lizardite (Weber and Greer 1965; Govier and Arnold 2004; McKelvy et al. 2006), especially at high temperature. Considering the relatively low HD formation enthalpy of the structure containing 0.8125 wt% HD, this structure was used as the model in further studies on the properties of HD-bearing lizardite.

## High $P$–$T$ stability and ionic transport property

FPMD is proved a good method in investigating crystal properties under conditions of high $P$–$T$ and the mean-square displacement (MSDs) results are often applied to analyze crystal stability (Bühl and Kabrede 2006). The MSDs of H, O, Mg, and Si of lizardite and 0.8125 wt% HD-bearing lizardite fluctuated slightly (Fig. 3a, b) at temperatures of 500, 700, and 900 K and the balanced pressure shown in Table 2. The MSDs' results indicated that all the atoms of lizardite and 0.8125 wt% HD-bearing lizardite are vibrating around the crystal lattice and no obvious diffusion of these atoms occurred under high $P$–$T$ conditions. Our FPMD results suggest that lizardite and 0.8125 wt% HD-bearing lizardite
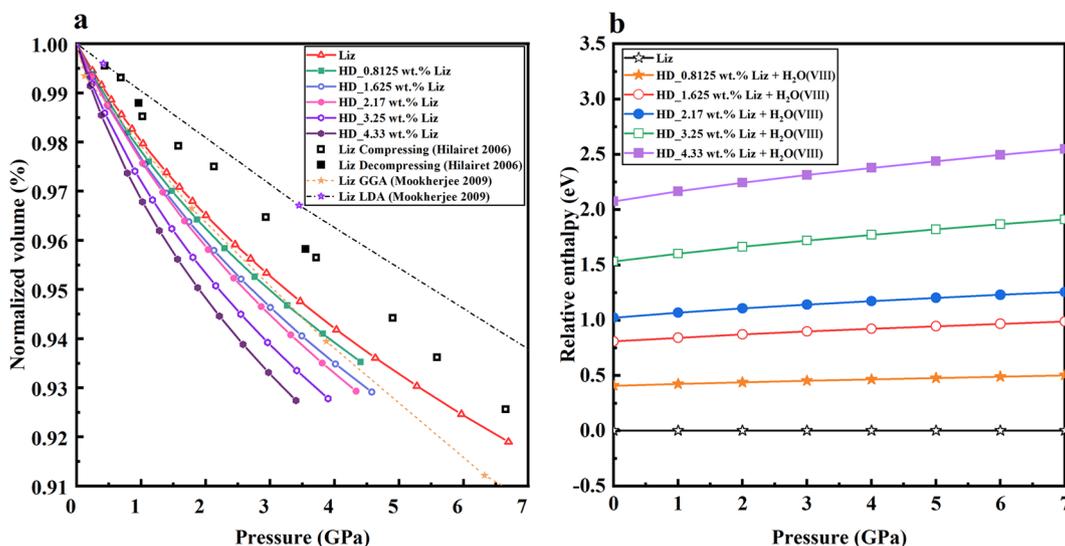


**Fig. 2** **a** Normalized pressure–volume relations of lizardite with different HD concentrations at 0 K. Black open squares show the compressing experiment of lizardite; the black filled squares show the decompressing experiment of lizardite (Hilairet et al. 2006). **b** Relative HD formation enthalpies as a function of pressure at 0–7 GPa. Open stars represent lizardite, while full stars, open circles, full circles, open squares, and full squares denote lizardite with 0.8125 wt%, 1.625 wt%, 2.17 wt%, 3.25 wt%, and 4.33 wt% HD
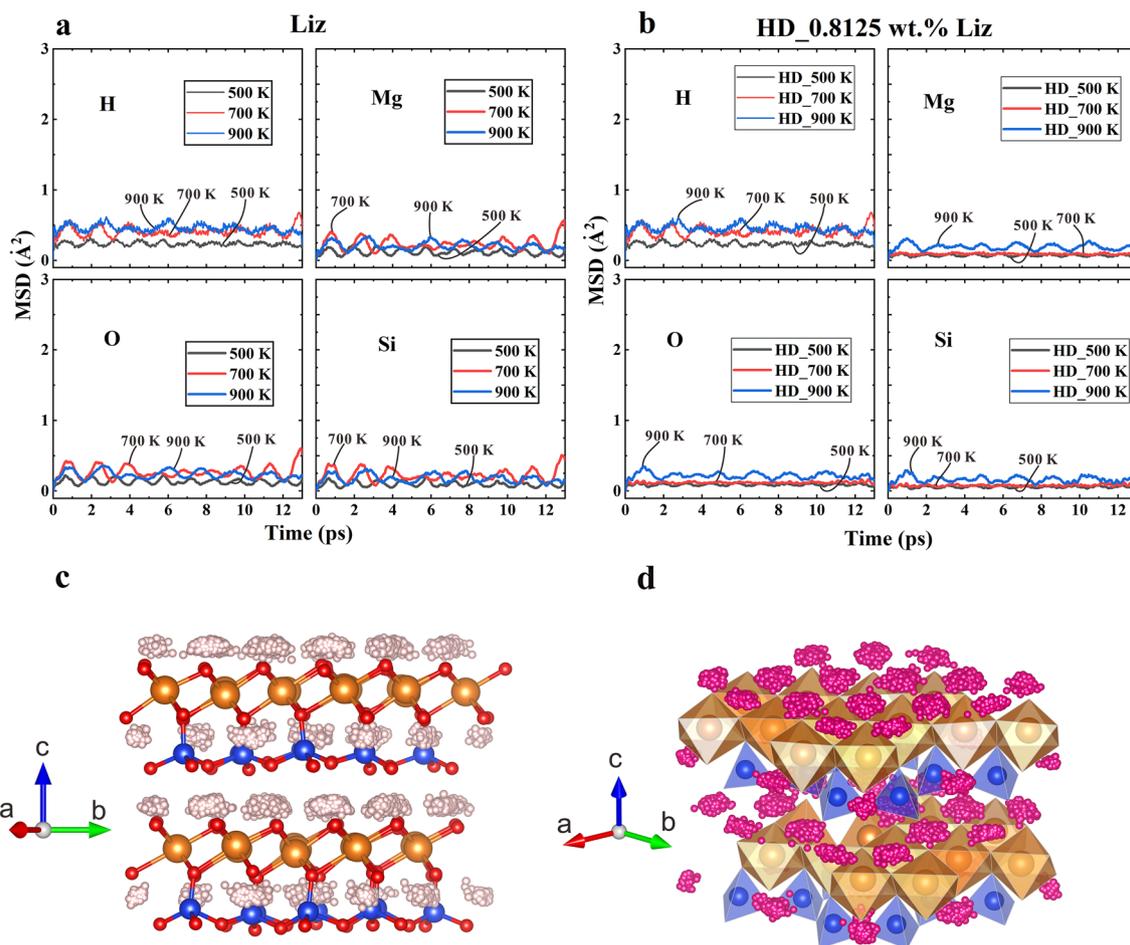
**Fig. 3** Comparison of ion migration behavior in lizardite with and without HD. **a, b** Calculated mean-square displacements (MSDs) of H⁺, O²⁻, Mg²⁺, and Si⁴⁺ of lizardite and 0.8125 wt% HD-bearing lizardite at 500, 700, and 900 K. **c** Trajectories of proton in lizardite. Pink, red, golden, and blue spheres represent H, O, Mg, and Si atoms, retrospectively. **d** Trajectories of proton in 0.8125 wt% HD-bearing lizardite. Magenta spheres denote H atoms, golden sheets represent Mg-O octahedra polyhedral, and blue sheets represent Si–O tetrahedra polyhedral

**Table 2** Balanced pressure of FPMD simulation of lizardite and 0.8125 wt% HD-bearing lizardite at 500, 700, and 900 K

| Temperature (K) | 500 | 700 | 900 | 500[a] | 700[a] | 900[a] |
|---|---|---|---|---|---|---|
| Pressure (GPa) | 1.54 | 1.38 | 1.70 | 1.25 | 1.24 | 1.25 |

[a]Temperature with mark represents the case of 0.8125 wt% HD-bearing lizardite

are stable at 500, 700, and 900 K, and the balanced pressure around 1 GPa to 2 GPa. Therefore, lizardite with HD concentration lower than 0.8125 wt% shows high thermal stability and can be present in the crust and upper mantle.

Nominal anhydrous minerals with hydrogen impurities have already been proved to have great influence on electric conductivity (Karato 1990; Wang et al. 2006), while the electrical conductivity and micro-conductance mechanism of hydrous minerals have not yet been clearly figured out. Previous impedance spectroscopy experiments of

serpentine (Zhu et al. 2001; Guo et al. 2011; Reynard et al. 2011) have yielded results that differ by several orders of magnitude, which could be attributed to the different sample containers used in experiments and the directional alignment of the sample. The consistence part of those experimental results is that serpentine shows low conductivity as an insulator at relatively low temperatures. The dominant conductance mechanism for Fe-free hydrous minerals is believed to be proton conduction (Guo et al. 2011). To confirm the electrical conductance mechanism

of proton migration, we investigated the proton conduction of lizardite and 0.8125 wt% HD-bearing lizardite, employing the FPMD simulation. As shown in Fig. 3, protons in lizardite with and without HD do not show obvious diffusion effect, as indicated from the MSDs (Fig. 3a, b) and trajectories (Fig. 3c, d). This suggests that proton conduction is not obvious at a wide range of temperature up to 900 K, at the balanced pressure ~ 1.25 GPa of HD-bearing lizardite and ~ 1.5 GPa of lizardite. These results are in convergence with the former conclusion derived from experiments (Zhu et al. 2001). Zhu investigated electrical conductivity of serpentine and eliminated the disturbance of highly conductive solid phases at low temperature. In their experiments, electrical conductivity of lizardite

is below $10^{-5}$ S/m at 573 K, and higher values for electrical conductivity are attributed to the presence of the highly conductive network of free water released during dehydration.

To figure out the main ionic transport mechanism of lizardite, we investigated two main migration channels (Fig. 4a) for protons. Figure 4 illustrates the proton migration barrier energy in lizardite at 0, 3, 7, and 10 GPa, respectively. As pressure increases from 0 to 10 GPa, the barrier energies decrease progressively from 1.22 to 1.07 eV along Path I (Fig. 4b), while the barrier energy along Path II drops rapidly from 5.56 to 3.42 eV and then stabilize with the pressure increasing, as shown in Fig. 4c. We also calculated the



**Fig. 4** **a** Two main proton migration channels Path I and Path II of lizardite. **b, c** Proton migration barrier energies in lizardite under pressure of 0, 3, 7, and 10 GPa. Path I: migration within the layer gap between octahedral and tetrahedral sheets and vertical with <001> direction. Path II: migration along <001> direction and cross the layer gap
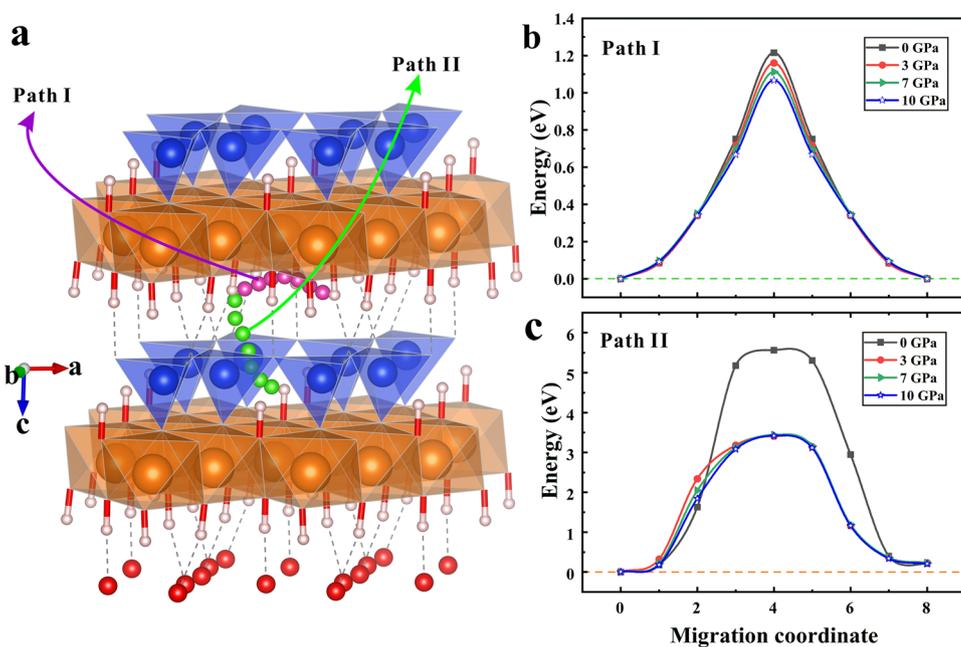
**Table 3** Elastic constants of lizardite

| P (GPa) | 0 | 1 | 2 | 3 | 4 | 5 | 6 | 7 |
|---|---|---|---|---|---|---|---|---|
| $C_{11}$ (GPa) | 215.6 (212.6) | 221.3 | 225.1 (222.1) | 231.1 | 234.6 (228.4) | 237.4 | 243.1 (231.2) | 245.8 |
| $C_{33}$ (GPa) | 58.3 (57.3) | 83.9 | 100.6 (102.6) | 119.4 | 136.4 (133.6) | 148.9 | 163.0 (159.4) | 166.2 |
| $C_{44}$ (GPa) | 15.4 (11.6) | 15.9 | 22.5 (13.4) | 18.3 | 16.2 (13.5) | 14.5 | 15.9 (12.6) | 13.6 |
| $C_{66}$ (GPa) | 70.2 (69.7) | 71.2 | 73.0 (71.9) | 74.0 | 73.0 (73.5) | 75.7 | 74.4 (74.7) | 76.0 |
| $C_{12}$ (GPa) | 75.3 (73.3) | 79.1 | 82.3 (78.5) | 84.9 | 88.6 (82.1) | 89.6 | 94.4 (81.8) | 93.9 |
| $C_{13}$ (GPa) | 8.7 (8.5) | 16.4 | 20.2 (21.6) | 26.0 | 34.1 (34.5) | 38.5 | 43.4 (48.1) | 54.9 |
| $C_{14}$ (GPa) | −2.0 (1.3) | −2.2 | −2.3 (1.7) | −2.8 | −2.7 (1.6) | −2.7 | −3.3 (1.9) | −4.2 |
| $\rho$ (g/cm³) | 2.493 | 2.540 | 2.581 | 2.619 | 2.650 | 2.677 | 2.703 | 2.729 |
| $V_{\emptyset}$ (km/s) | 4.91 | 5.34 | 5.54 | 5.81 | 6.03 | 6.15 | 6.33 | 6.49 |
| $V_{p}$ (km/s) | 6.23 | 6.60 | 6.60 | 7.16 | 7.19 | 7.24 | 7.44 | 7.50 |
| $V_{s}$ (km/s) | 3.84 | 3.89 | 3.89 | 4.18 | 3.91 | 3.83 | 3.90 | 3.76 |

$C_{ij}$ values presented in the bracket were obtained from previous GGA results (Tsuchiya 2013a)

**Table 4** Elastic constants of lizardite with 0.8125 wt% $H_2O$ vacancies

| P (GPa) | 0 | 1 | 2 | 3 | 4 | 5 | 6 | 7 |
|---|---|---|---|---|---|---|---|---|
| $C_{11}$ (GPa) | 207.2 | 215.2 | 219.4 | 222.5 | 228.0 | 234.8 | 237.1 | 241.7 |
| $C_{22}$ (GPa) | 206.8 | 214.2 | 218.3 | 224.0 | 229.2 | 235.1 | 237.6 | 240.8 |
| $C_{33}$ (GPa) | 43.5 | 70.7 | 92.2 | 109.9 | 121.0 | 132.4 | 141.6 | 149.5 |
| $C_{44}$ (GPa) | 10.3 | 11.4 | 12.8 | 13.8 | 14.4 | 16.0 | 14.2 | 13.0 |
| $C_{55}$ (GPa) | 9.4 | 12.2 | 14.9 | 13.4 | 14.7 | 12.9 | 13.6 | 13.0 |
| $C_{66}$ (GPa) | 67.0 | 68.3 | 69.4 | 70.3 | 71.3 | 72.7 | 72.9 | 73.9 |
| $C_{12}$ (GPa) | 74.2 | 79.6 | 81.0 | 83.2 | 86.2 | 91.8 | 92.6 | 95.2 |
| $C_{13}$ (GPa) | 5.3 | 12.8 | 17.6 | 23.6 | 30.7 | 33.8 | 42.6 | 46.3 |
| $C_{14}$ (GPa) | − 1.1 | − 1.4 | − 1.4 | − 1.7 | − 1.7 | − 2.1 | − 1.6 | − 2.1 |
| $C_{15}$ (GPa) | − 0.5 | 0.2 | − 0.7 | − 0.2 | − 0.4 | − 0.3 | 0.7 | 0.1 |
| $C_{16}$ (GPa) | 0.2 | 0.3 | 0 | 0.1 | 0.3 | 0 | − 0.5 | − 0.4 |
| $C_{23}$ (GPa) | 7.8 | 13.2 | 19.9 | 25.7 | 32.3 | 34.6 | 42.7 | 47.4 |
| $C_{24}$ (GPa) | 1.8 | 1.8 | 2.0 | 2.9 | 2.7 | 3.7 | 3.0 | 2.7 |
| $C_{25}$ (GPa) | 0.2 | 0.5 | 0.3 | 0.6 | 0.4 | 0.1 | 1.0 | 1.0 |
| $C_{26}$ (GPa) | − 0.4 | − 0.3 | − 0.5 | − 0.5 | − 0.4 | − 0.5 | 0.7 | − 0.5 |
| $C_{34}$ (GPa) | 0.2 | − 0.2 | 0.1 | 0.6 | 0.2 | 1.1 | 1.9 | 1.9 |
| $C_{35}$ (GPa) | − 0.8 | 0.1 | 0 | − 0.6 | − 0.6 | − 0.6 | 0.7 | − 0.1 |
| $C_{36}$ (GPa) | − 0.4 | − 0.1 | − 0.4 | 0 | 0.1 | 0.2 | 0 | 0.4 |
| $C_{45}$ (GPa) | 0.3 | 1.0 | 0.1 | 0.5 | 0.6 | 0.6 | 0.4 | 0.8 |
| $C_{46}$ (GPa) | − 0.1 | − 0.4 | − 0.6 | − 0.5 | − 0.7 | − 0.5 | − 0.5 | − 0.7 |
| $C_{56}$ (GPa) | − 0.9 | − 1.3 | − 1.6 | − 1.9 | − 2.3 | − 1.9 | − 2.5 | − 2.5 |
| $\rho$ (g/cm$^3$) | 2.455 | 2.511 | 2.555 | 2.591 | 2.624 | 2.655 | 2.685 | 2.712 |
| $V_\emptyset$ (km/s) | 4.64 | 5.13 | 5.44 | 5.68 | 5.88 | 6.02 | 6.18 | 6.29 |
| $V_p$ (km/s) | 5.82 | 6.30 | 6.62 | 6.82 | 7.00 | 7.12 | 7.24 | 7.30 |
| $V_s$ (km/s) | 3.51 | 3.65 | 3.77 | 3.77 | 3.81 | 3.81 | 3.76 | 3.71 |
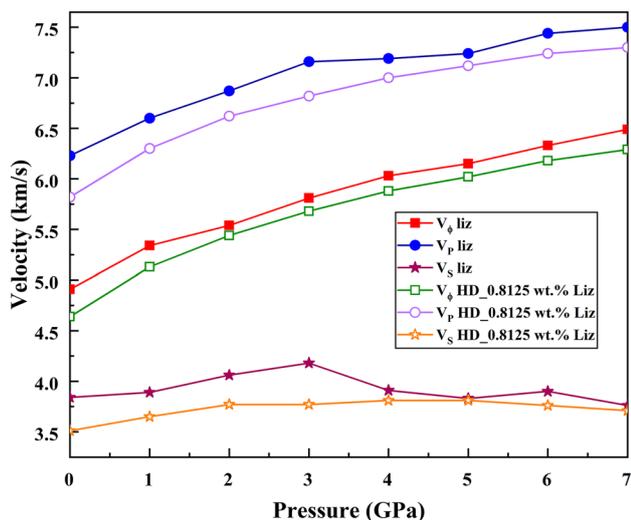


**Fig. 5** Seismic velocities of lizardite and lizardite with 0.8125 wt% HD. Full circles denote primary wave velocity of lizardite, full squares represent bulk sound velocity of lizardite, and full stars denote shear wave velocity of lizardite. For lizardite with 0.8125 wt% HD, open circles show primary wave velocity, open squares denote bulk sound velocity, and open stars represent shear wave velocity

migration barrier energies of $Mg^{2+}$ (5.4 eV, 2.56 GPa) and $Si^{4+}$ (9.4 eV, 2.56 GPa). These results suggest that the dominant ionic transportation mechanism in lizardite is proton migration within the layer.

## Seismic velocities and anisotropy

Using the finite strain method within DFT calculation, the elastic constants of lizardite and 0.8125 wt% HD-bearing lizardite under pressure are calculated and listed in Tables 3 and 4. Accordingly, we calculated the $V_P$, $V_S$. and $V_\emptyset$ using the Vioet–Ruess–Hill scheme (Voigt 1928; Reuss 1929; Hill 1952), as shown in Fig. 5.

For lizardite with 0.8125 wt% HD, notably declines of $V_P$, $V_S$ and $V_\emptyset$ were observed and exhibited in Fig. 5. Due to the presence of HD, $V_P$ decreases by 6.58%, 4.54%, 4.74%, and 2.64%, and $V_S$ decreases by 8.59%, 6.17%, 9.81%, and 2.56 and $V_\emptyset$ decreases by 5.49%, 3.93%, 2.24%, and 2.48% at 0, 1, 3, and 4 GPa, respectively.

In addition, we calculated the P-wave anisotropy and S-wave anisotropy at 3 GPa with the calculated elastic constants, as shown in Fig. 6. 0.8125 wt% HD of lizardite leads to significant increasing of seismic velocity anisotropy for
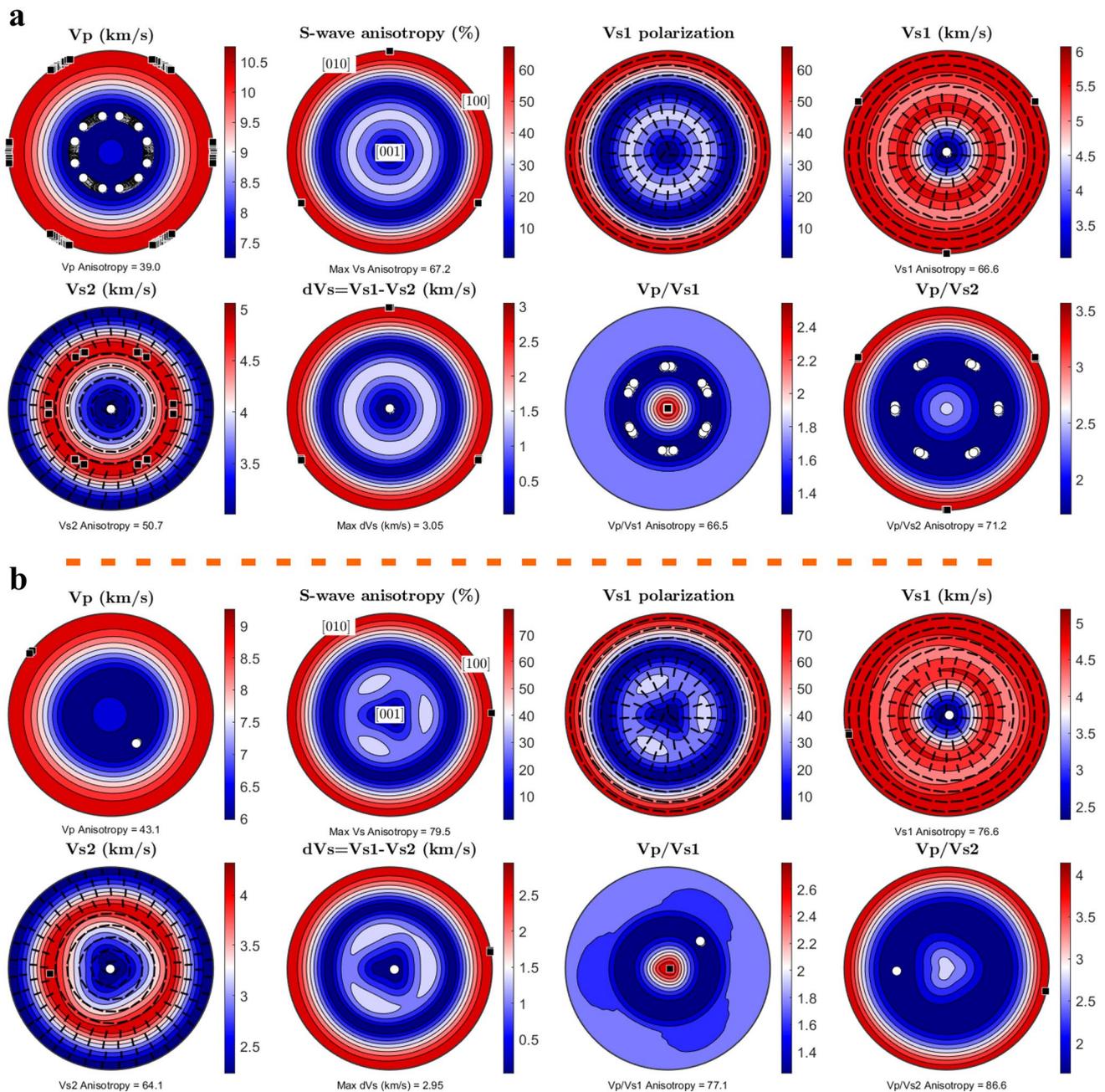
**Fig. 6** Elastic anisotropy of lizardite and 0.8125 wt% HD-bearing lizardite at 3 GPa. Black squares mark the maximum, and the white circles mark minimum. **a** Lizardite. **b** Lizardite with 0.8125 wt%

$H_2O$ vacancies. $V_P$, $V_{S1}$. and $V_{S2}$ of different vibration and propagation directions were obtained by solving Christoffel equation employing MTEX (Mainprice et al. 2011)

lizardite. The $V_P$ and $V_S$ anisotropies of lizardite with 0.8125 wt% HD is 9.5% and 15.6% higher than those of lizardite without HD. The calculated $AV_P$, $AV_{S1}$, $AV_{S2}$, and max $AV_S$ of lizardite and lizardite with 0.8125 wt% HD at 0-7 GPa are shown in Fig. 7. With the increasing of pressure, P-wave anisotropy $AV_P$ quickly decreases, while S-wave anisotropy $AV_{S1}$ fluctuates and $AV_{S2}$ steadily increases. The obvious seismic velocity anisotropy differences of lizardite and

HD-bearing lizardite can be seen in Fig. 7. In general, the differences decrease with applied pressure. The max $AV_S$ of 0.8125 wt% HD-bearing lizardite increases by 19.37%, 16.40%, 21.28%, and 15.43% at the pressure of 0, 1, 2, and 3 GPa, respectively. Our results suggest that the seismic velocity anisotropies of lizardite are quite sensitive to HD. A small amount of $H_2O$ defects in lizardite can obviously change its seismic velocity anisotropy. It indicates that the
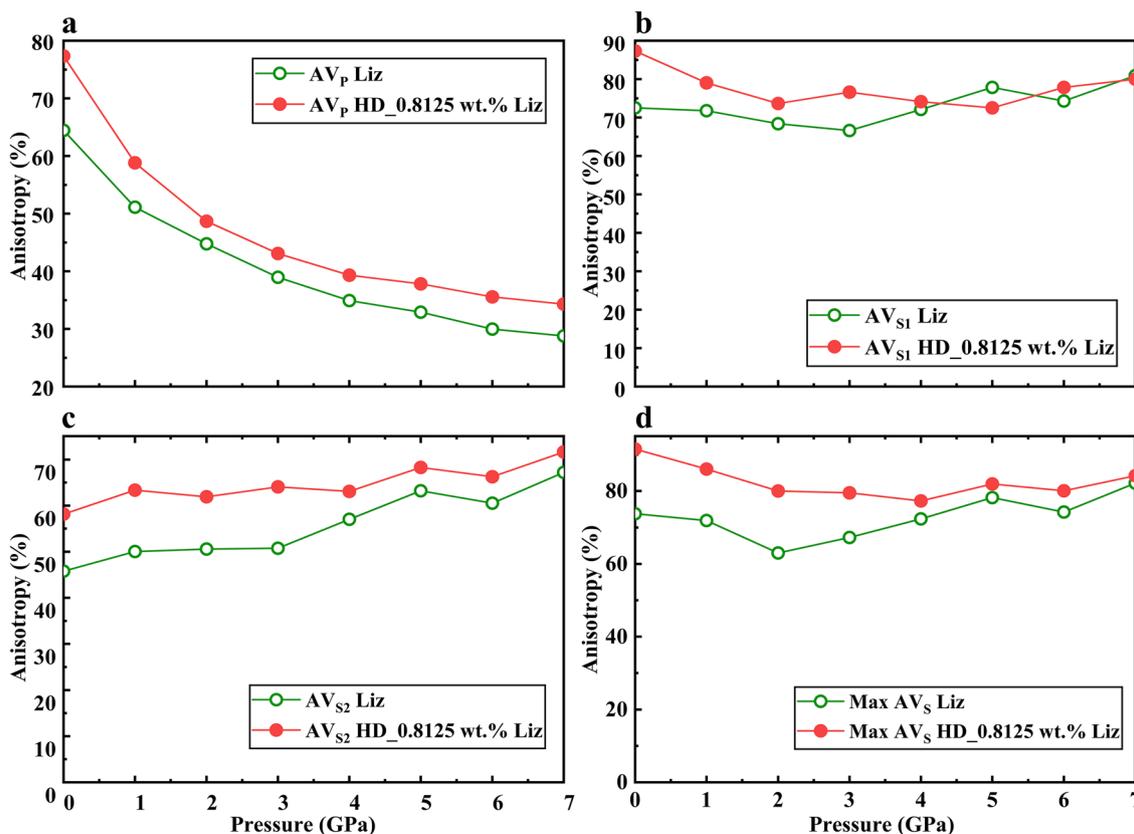
**Fig. 7** Seismic velocity anisotropy as a function of pressure at 0–7 GPa. **a** P-wave anisotropy. **b** Anisotropy of fast S-wave velocities. **c** Anisotropy of slow S-wave velocities. **d** The max $AV_S$ of lizardite and 0.8125 wt% HD-bearing lizardite. Red curve denotes lizardite, and green curve denotes lizardite with 0.8125 wt% HD
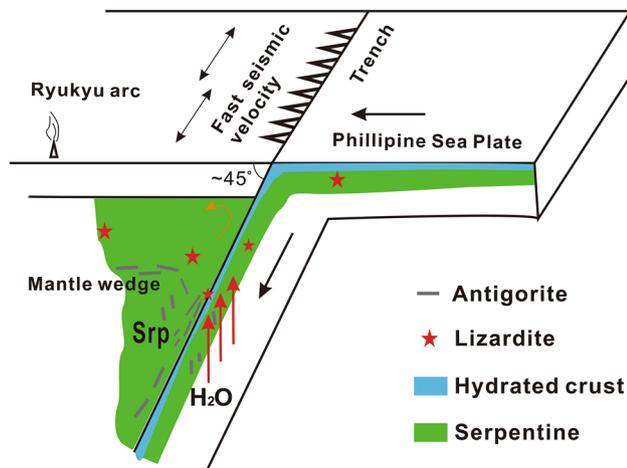


**Fig. 8** Schematic cross-section through the Ryukyu arc. The red stars represent lizardite or HD-bearing lizardite; the gray segments represent antigorite

seismic velocity anisotropy will increase when HD concentrations in lizardite increase at high temperature or during dehydration process (Fig. 8).

## Geological implications

A low-velocity structure has been identified beneath the northeast Ryukyu arc at a depth of 50 km (~ 1–2 GPa) (Nakamura et al. 2003). This is consistent with the high-resolution 3 D P-wave velocity structure determined by seismic inversion of data observed in Kyushu, Okinawa Trough, Taiwan, and Fujian province of China (Wang et al. 2008). Simultaneously, a delay of 1–2 s between the fast splitting shear wave and slow splitting shear wave was observed in the Ryukyu arc (Long and van der Hilst 2006), while 0.1–0.2 s delay was observed in northeast Japan (Nakajima and Hasegawa 2004; Nakajima et al. 2006), indicating the high S-wave anisotropy parallel to the trench. The anomalously low seismic velocities are attributed to the aqueous fluid and partial melting that produced extensive dehydration reactions within the subducting slab (Wang et al. 2008; Peacock 1990; Iwamori 1998). The anisotropy parallel to the trench is difficult to explain in terms of Olivine, and the applied model of serpentine significantly increased the anisotropy with a much thinner anisotropic layer (Katayama et al. 2009). Antigorite shows notable differences of $V_{S1}$ and $V_{S2}$ as the incidence angle changes from 0°, (100) direction, to 90°, (001). The crystal
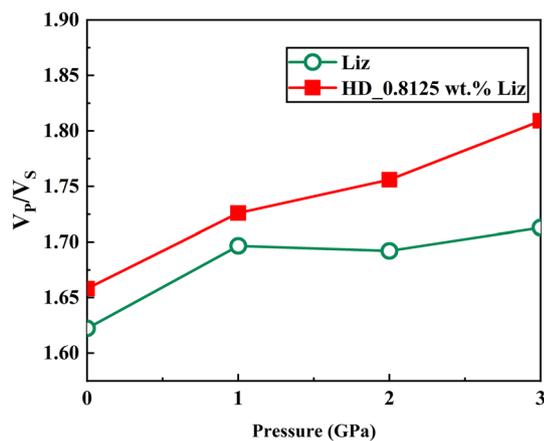
**Fig. 9** $V_P/V_S$ values as a function of pressure of lizardite and 0.8125 wt% HD-bearing lizardite

preferred orientation (CPO) characteristics of antigorite have been frequently applied in explaining high S-wave anisotropy (Katayama et al. 2009; Mookherjee and Capitani 2011; Campione and Capitani 2013). To generate the large delay time of 1–2 s, the "mantle wedge hydration" model (Mookherjee and Capitani 2011) explains the difference in terms of heterogenous distribution of antigorite using the CPO characteristic that antigorite shows high $AV_S$ in relative low incidence angle. However, the incidence angles have to be confined by $V_P$ and the lower $V_P$ corresponds to higher incidence angle and the lower $AV_S$ of antigorite (Mookherjee and Capitani 2011). For instance, the observed $V_P$ ranges between 6.7 and 7.2 km/s in the Kanto district of Japan (Seno et al. 2001), while the $AV_S$ changes from 35 to 37% and the derived value of $V_P/V_S$ (1.6) is significantly lower than the observed value (1.73–1.84) (Christensen 2004).

At 3 GPa ($6.67 < V_P < 7.2$ km/s), the calculated $V_P/V_S$ of lizardite is 1.71, while $V_P/V_S$ of HD-bearing lizardite is 1.81 (Fig. 9). Both values are higher than those for antigorite (Mookherjee and Capitani 2011) and are close to the observed values. Lizardite shows similar CPO characteristics to antigorite and HD-bearing lizardite presents higher azimuthal anisotropy. The 0.8125 wt% HD-bearing lizardite are as much as five times stronger than that for olivine ($AV_s$ of $\sim$ 18%) (Abramson et al. 1997). Thus, lizardite, especially with HD, is able to enhance the trench parallel anisotropy, and should be associated with the low-velocity anomalies. The subducting slab beneath Ryukyu arc is quite old (~50 Ma; Seno 1988) and lizardite can present within the forearc mantle wedge. The silica-saturated hydrated crust is likely to stabilize layered hydrous minerals (Peacock and Hyndman 1999). Lizardite can be partially dehydrated and gradually changes into antigorite and/or olivine in relatively shallow regions (Reynard et al. 2011). The geological structure and heterogeneity of lizardite may influence the P- and S-wave velocities and CPO properties, which could be used to analyze seismic events and explain observed seismic anomalies.

## References

Abramson E, Brown J, Slutsky L, Zaug J (1997) The elastic constants of San Carlos olivine to 17 GPa. J Geophys Res 102:12253–12263

Anderson D (1989) Theory of the earth blackwell scientific. Mass, Boston

Auzende A, Guillot S, Devouard B, Baronnet A (2006) Behaviour of serpentinites in convergent context: microstructural evidence. Eur J Mineral 18:21–33

Auzende A, Escartin J, Walte N, Guillot S, Hirth G, Frost D (2015) Deformation mechanisms of antigorite serpentinite at subduction zone conditions determined from experimentally and naturally deformed rocks. Earth Planet Sci Lett 411:229–240

Brindley G, Zussman J (1957) A structural study of the thermal transformation of serpentine minerals to forsterite. Am Miner 42(7–8):461–474

Bühl M, Kabrede H (2006) Acidity of Uranyl (VI) Hydrate Studied with first-principles molecular dynamics simulations[J]. ChemPhysChem 7(11):2290–2293

Campione M, Capitani G (2013) Subduction-zone earthquake complexity related to frictional anisotropy in antigorite[J]. Nature Geosci 6(10):847

Caruso L, Chernosky J (1979) The stability of lizardite. Can Mineral 17(4):757–769

Christensen N (2004) Serpentinites, peridotites, and seismology. Int Geol Rev 46(9):795–816

Dlugogorski B, Balucan R (2014) Dehydroxylation of serpentine minerals: implications for mineral carbonation. Renew Sustain Energy Rev 31:353–367

Dungan M (1979) A microprobe study of antigorite and some serpentine pseudomorphs. Can Mineral 17:771–784

El-Salaam K, Gabr R, Said A (1979) Sintering studies on Mg (OH) 2. Surf Technol 9(6):427–433

Evans B (1977) Metamorphism of alpine peridotite and serpentinite. Ann Rev Earth Planet Sci 5:397–447

Evans B (2004) The serpentinite multisystem revisited: chrysotile is metastable. Int Geol Rev 46:479–506

Freund F, Sperling V (1976) A magnesium oxide defect structure of N ~ Yagonal symmetry. Mat Res Bull 11:621–630

Frost B (1975) Contact metamorphism of serpentinite, chloritic blackwall and rodingite at Paddy-Go-Easy Pass. Central Cascades, Washington. l. Petrologp 16:272–313

Govier D, Arnold M (2004) Quantitative differential thermal analysis of antigorite and lizardite serpentine. Internal Report, Albany Research Center Analytical Laboratory

Guo X, Yoshino T, Katayama I (2011) Electrical conductivity anisotropy of deformed talc rocks and serpentinites at 3 GPa. Phys Earth Planet Inter 188:69–81

He Yu, Sun Yang, Xia Lu, Gao Jian, Li Hong, Li Heping (2016) First-principles prediction of fast migration channels of potassium ions in KAlSi3O8 hollandite: implications for high conductivity anomalies in subduction zones. Geophys Res Lett 43:6228–6233

Henkelman G, Uberuaga B, Jonsson H (2000) A climbing image nudged elastic band method for finding saddle points and minimum energy paths. J Chem Phys 113:9901–9904

Hilairet N, Daniel I, Raynard B (2006) P-V equation of state and the relative stabilities of serpentine varieties. Phys Chem Minerals 33:629–637

Hill R (1952) The elastic behaviour of a crystalline aggregate. Proc Phys Soc Sect A 65:349

Hyndman R, Peacock S (2003) Serpentinization of the forearc mantle. Earth Planet Sci Lett 212:417–432

Iwamori H (1998) Transportation of $H_2O$ and melting in subduction zones. Earth Planet Sci Lett 160:65–80

Karato S (1990) The role of hydrogen in the electrical conductivity of the upper mantle[J]. Nature 347(6290):272

Karki B, Stixrude L, Clark S, Warren M, Ackland G, Crain J (1997) Structure and elasticity of MgO at high-pressure. Am Mineral 82:51–60

Karki B, Stixrude L, Wentzcovitch R (2001) High-pressure elastic properties of major minerals of the Earth's mantle from first-principles. Rev Geophys 39:507–534

Katayama I, Hirauchi K, Michibayashi K, Ando J (2009) Trench-parallel anisotropy produced by serpentine deformation in the hydrated mantle wedge[J]. Nature 461(7267):1114

Kohn W, Sham L (1965) Self-consistent equations including exchange and correlation effects. Phys Rev A 140:1133–1138

Kresse G, Furthmüller J (1996) Efficient iterative schemes for ab initio total-energy calculations using a plane-wave basis set. Phys Rev B 54:11169–11186

Long M, van der Hilst R (2006) Shear wave splitting from local events beneath the Ryukyu arc: trench-parallel anisotropy in the mantle wedge[J]. Phys Earth Planet Inter 155(3–4):300–312

Mainprice D, Hielscher R, Schaeben H (2011) Calculating anisotropic physical properties from texture data using the MTEX open-source package[J]. Geol Soc Lond Spec Publ 360(1):175–192

McKelvy M, Sharma R, Chizmeshya A, Carpenter R, Streib K (2001) Magnesium hydroxide dehydroxylation: in situ nanoscale observations of lamellar nucleation and growth. Chem Mater 13(3):921–926

McKelvy M, Chizmeshya A, Squires K, Carpenter R, Béarat H (2006) A novel approach to mineral carbonation: enhancing carbonation while avoiding mineral pretreatment process cost. Arizona State University, Tempe

Mellini M, Zanazzi P (1989) Effects of pressure on the structure of lizardite-1T. Eur J Mineral 1:13–19

Mookherjee M, Capitani G (2011) Trench parallel anisotropy and large delay times: elasticity and anisotropy of antigorite at high pressures[J]. Geophys Res Lett 38:L09315

Mookherjee M, Mainprice D (2014) Unusually large shear wave anisotropy for chlorite in subduction zone settings. Geophys Res Lett 41:1506–1513

Mookherjee M, Stixrude L (2009) Structure and elasticity of serpentine at high-pressure. Earth Planet Sci Lett 279:11–19

Mookherjee M, Tsuchiya J (2015) Elasticity of superhydrous phase, B, Mg10Si3O14 (OH) 4[J]. Phys Earth Planet Inter 238:42–50

Nakajima J, Hasegawa A (2004) Shear-wave polarization anisotropy and subduction-induced flow in the mantle wedge of northeastern Japan. Earth Planet Sci Lett 225:365–377

Nakajima J, Shimizu J, Hori S, Hasegawa A (2006) Shear-wave splitting beneath the southwestern Kurile arc and northeastern Japan arc. Geophys Res Lett 33:L05305

Nakamura M, Yoshida Y, Zhao D, Katao H, Nishimura S (2003) Three-dimensional P- and S-wave velocity structures beneath the Ryukyu arc. Tectonophysics 369:121–143

Padrón-Navarta J, Tommasi A, Garrido C, Lopez Sanchez V, Gomez-Pugnaire M, Jabaloy A, Vauchez A (2010) Fluid transfer into the wedge controlled by high-pressure hydrofracturing in the cold top-slab mantle. Earth Planet Sci Lett 297:271–286

Peacock S (1990) Fluid processes in subduction zones. Science 248:329–337

Peacock SM, Hyndman RD (1999) Hydrous minerals in the mantle wedge and the maximum depth of subduction thrust earthquakes. Geophys Res Lett 26(16):2517–2520

Perdew J, Zunger A (1981) Self-interaction correction to density functional approximations for many-electron systems. Phys Rev B 23:5048–5079

Reuss A (1929) Berechnung der Fliebgrenze von Mischkristallen auf Grund der Plastizita¨tsbedingung fu¨ r Einkristalle. Z Angew Math Mech 9:49–58

Reynard B (2013) Serpentine in active subduction zones. Lithos 178:171–185

Reynard B, Mibe K, Van de Moortele B (2011) Electrical conductivity of the serpentinised mantle and fluid flow in subduction zones. Earth Planet Sci Lett 307:387–394

Schwartz S, Guillot S, Reynard B, Lafay R, Debret B, Nicollet C, Auzende A (2013) Pressure–temperature estimates of the lizardite/antigorite transition in high pressure serpentinites[J]. Lithos 178:197–210

Seipold U, Schilling F (2003) Heat transport in serpentinites. Tectonophysics 370(1–4):147–162

Seno T (1988) Tectonic evolution of the west Philippine basin[J]. Modern Geology 12:481–495

Seno T, Zhao D, Kobayashi Y, Nakamura M (2001) Dehydration of serpentinized slab mantle: seismic evidence from southwest Japan. Earth Planet Space 53(9):861–871

Tsuchiya J (2013a) A first-principles calculation of the elastic and vibrational anomalies of lizardite under pressure. Am Mineral 98(11–12):2046–2052

Tsuchiya J (2013b) First principles prediction of a new high-pressure phase of dense hydrous magnesium silicates in the lower mantle. Geophys Res Lett 40(17):4570–4573

Tsuchiya J, Tsuchiya T (2009a) Elastic properties of δ-AlOOH under pressure: first principles investigation. Phys Earth Planet Inter 174(1–4):122–127

Tsuchiya J, Tsuchiya T (2009b) First-principles investigations on the elastic and vibrational properties of hydrous wadsleyite under pressure. Geochimica et Cosmochimica Acta Supplement 73:A1350

Tsuchiya J, Tsuchiya T, Tsuneyuki S, Yamanaka T (2002) First principles calculation of a high-pressure hydrous phase, δ-AlOOH. Geophys Res Lett 29(19):15-1

Tsuchiya J, Tsuchiya T, Tsuneyuki S (2005) First-principles study of hydrogen bond symmetrization of phase D under high pressure. Am Mineral 90(1):44–49

Tyburczy J, Duffy T, Ahrens T, Lange M (1991) Shock wave equation of state of serpentine to 150 GPa: implications for the occurrence ofwater in the Earth's lower mantle. J Geophys Res 96:18011–18027

Voigt W (1928) Lehrbuch der kristallphysik[M]. Leipzig, Teubner, pp 962

Wang D, Mookherjee M, Xu Y et al (2006) The effect of water on the electrical conductivity of olivine[J]. Nature 443(7114):977

Wang Z, Huang R, Huang J et al (2008) P-wave velocity and gradient images beneath the Okinawa Trough[J]. Tectonophysics 455(1–4):1–13

Weber J, Greer R (1965) Dehydration of serpentine: heat of reaction and reaction kinetics at PH 2 O = 1 ATM. Am Miner 50(3–4):450–464

Whittaker E, Zussman J (1956) The characterization of serpentine minerals by X-ray diffraction. Mineral Mag J Mineral Soc 31(233):107–126

Zhu M, Xie H, Guo J, Bai W, Wu Z (2001) Impedance spectroscopy analysis on electrical properties of serpentine at high pressure and high temperature. Sci China Ser D-Earth Sci 44:336–345